Computers and Electronics in Agriculture 118 (2015) 204–214

Contents lists available at ScienceDirect

Computers and Electronics in Agriculture

journal homepage: www.elsevier.com/locate/compag

An automated method for tree-ring delineation based on active contours guided by DT-CWT complex coefficients in photographic images: Application to *Abies alba* wood slice images

Pol Kennel [a,b,*], Philippe Borianne [a], Gérard Subsol [b]

[a] Agricultural Research for Development, UMR AMAP, F-34398 Montpellier, France
[b] Laboratory of Informatics, Robotics and Microelectronics, ICAR Team, CNRS/University Montpellier, F-34000 Montpellier, France

ARTICLE INFO

Article history:
Received 13 March 2015
Received in revised form 6 September 2015
Accepted 8 September 2015

Keywords:
Tree-ring delineation
Active contour
Dual-tree complex wavelet transform
Dendrochronology

ABSTRACT

This paper describes an efficient method for delineating tree-rings and inter tree-rings in wood slice images. The method is based on an active contour approach and a multi-scale gradient map resulting from the Dual Tree Complex Wavelet Transform (DT-CWT). The method is automated and does not require any pith localization. It is also quite robust to some defect structures such as branch prints, cracks, knots or mold. We applied the method to process entire *Abies alba* wood slices (aged from 10 to 50 years) from bark to pith, which amounted to about 200 tree-rings. Our automatic delineation method performed accurately compared to the manual expert measurements with a mean *F*-score of 0.91 for the quality of delineation.

1. Introduction

In temperate trees, wood production by the cambium is rhythmic, with a new layer of wood being added each year. This iterative wood production process generates a set of circular shapes on the cross-sectional plane of a stem which are called "tree-rings". Tree-ring boundaries are visible thanks to a difference of wood density in the ring. More specifically, late wood on the outer portion of the ring is darker and denser than the early wood formed on the inner portion of the ring. The study of tree-rings is a common and fundamental part of dendrology and helps to understand, quantify and model secondary tree growth (MacDonald, 1998).

In most cases, one-dimensional radial intensity profiles (from bark to pith) of photographic images of a wood slice are used to detect tree-ring boundaries. This allows one to calculate the tree age and to obtain valuable information on its environmental conditions such as climate or forest dynamics (MacDonald, 1998). Nevertheless, if we want to study the growth process of the tree in greater depth, we need precisely to delineate the entire tree-ring areas in wood slices. Thus, the width and density (in numbers) of tree-rings show how biomass is allocated in the woody material, resulting in valuable information about wood quality, especially strength and stiffness (Hanning et al., 2003). Tree-ring surfaces can be used for geometrical measurements, which can be related to mechanical properties of the wood. For example, asymmetric growth will result in non-circular and irregularly spaced tree rings, which will characterize what is called reaction wood, which is a combination of compression and tension wood. Characterizing and quantifying wood tissues paves the way for 3-dimensional models of wood growth, which is an important issue for understanding biomass accumulation and carbon sequestration. All these parameters could help industrialists to predict whether a log is suitable for plywood, paper or plank making (Kumpulainen and Marjanen, 2010).

Some computer-aided methods have been proposed to count tree-rings and to give an estimation of their thickness in photographic images of wood slices. They can detect some parts of rings in a portion of an image, as in (Conner et al., 1998), by using an edge detector or detect intensity discontinuities along a ray defined from the pith to the bark, as in (Vaz et al., 2004; Norell, 2011), or the commercial software *WinDendro* (Regent Instruments, Canada[1]). While those techniques provide valuable parameters for dendrochronology applications, they do not lead to accurate segmentation and quantification of whole tree-rings. Other algorithms have been proposed to analyze the shape of the tree-ring structure in order to detect internal defects. For example, in

* Corresponding author at: Agricultural Research for Development, UMR AMAP, F-34398 Montpellier, France.
E-mail address: pol.kennel@gmail.com (P. Kennel).

[1] http://www.regentinstruments.com/assets/windendro_about.html.

http://dx.doi.org/10.1016/j.compag.2015.09.009
0168-1699/

(Bhandarkar et al., 2005) the authors proposed characterizing cracks by detecting lines making a significant non-zero angle with the rings. The method, based on an edge detector and line fitting procedure, provides efficient detection of the ring structure. Nevertheless, the rings themselves are not precisely delineated and, in particular, they are not closed.

In fact, few automatic techniques have been developed to delineate complete tree-rings precisely. Most of them first require detection of the pith, which is a key problem. For this purpose, in (Sjöberg et al., 2001) the authors proposed correlating a vector image (which more or less represents a local orientation) with an image characterizing an accumulation of concentric circles. The method described in (Chalifour et al., 2001) computes the gradient in a large number of randomly chosen pixels and approximates the pixel toward which all the gradient orientations point. In (Tadeusz et al., 2003), a center pixel is selected which enables conversion of the image into polar coordinates. When the center pixel corresponds to the pith, the polar image is formed by horizontal lines which can be easily characterized. In (Cerda et al., 2007), the center is defined as the pixel which minimizes an objective function and which fits all the points belonging to any detected edge to concentric circles. In (Borianne et al., 2010), the Hough transform is used to detect circles by using many diameter values. Once the pith is found, radial directions can be defined to enhance the intensity variations around the ring pixels as in (Borianne et al., 2010) or detect edges or intensity discontinuities as in (Chalifour et al., 2001; Sjöberg et al., 2001) or (Cerda et al., 2007). It is worth noting that in (Soille and Misson, 2001), there is no assumption on pith localization. The method is only based on latewood to earlywood transitions, which are detected using the Watershed algorithm. Another difficulty is to link the pixels that are detected as belonging to a tree-ring, in order to obtain a closed curve. Mathematical morphology operators such as erosion, dilation and skeletonization make it possible to fill holes and to produce one pixel width lines, as in (Sjöberg et al., 2001; Soille and Misson, 2001). In (Cerda et al., 2007), the authors propose working directly with a set of polygons which are concentrically included and whose vertices are pixels belonging to the rings. In (Borianne et al., 2010), it is a closed line that is directly fitted to some pixels tagged as "ring" points by using the active contour paradigm. This kind of method, which is widely used in image processing, was first described in a paper by (Kass et al., 1988), in which we can already find an application to wood slice photographs. Using a closed line directly solves the problem of linking isolated pixels and increases the robustness of the method with respect to local wood defects.

Our study once again addressed the question of using active contours to delineate concentric tree-rings.

Active contour models (also called "snakes") are often used to bridge the gap between low-level computer vision and high-level geometric representation. An active contour is a curve described within an image domain which can move under the effect of internal forces regularizing the shape of the curve, and external forces derived from the image attracting the curve toward some regions of interest. An active contour is often presented as an energy minimization model, which integrates a number of constraints derived from specific forces. Active contour models have been widely used in medical image processing (Cai et al., 2006; Nagappan et al., 2008), texture segmentation (Chen et al., 2006) or visual tracking (Paragios and Deriche, 2000). Active contour methods are quite difficult to classify, as shown in (McInerney and Terzopoulos, 1996; He et al., 2008), but we can define three major categories: parametric, implicit and point-based models. In the original parametric formulation (Kass et al., 1988), the optimal contour position was defined as that with the lowest sum of internal and external energies along the entire length of the contour. In this formulation, the continuous active contour cannot deal with changes in topology. Implicit formulation, introduced in (Caselles et al., 1993; Malladi et al., 1995), solved this problem. It consists, as in the level set formulation (Suri et al., 2002; Giraldi et al., 2006), in embedding the active contour as the zero level set of a higher dimensional function and in solving the corresponding motion equation. The main advantage of implicit representation is its ability to change the contour's topology during deformation. The main advantage of parametric representation is its effectiveness. For example, vertex sampling may not be constant or uniform on parametric contours, whereas resolution on implicit contours is constrained by the resolution of a regular grid. Implicit active contour models generally require considerable computational power, and parametric active contour models are difficult to set up and control. Simpler models based on a discrete set of points were therefore introduced. In (Gao et al., 1998), the point-based active contour consists of an ordered collection of points, called "*snaxels*", renowned for their simple implementation and usage. In the study described here, we opted for the point-based approach proposed in (Delingette and Montagnat, 2001), where a framework is defined for handling the active contour shape and topology in a simple and intuitive manner. The real issue is then to determine an efficient external force.

External forces are established in such a manner as to minimize the "energy" of the active contour. For image segmentation, the idea is to have low energy values around object boundaries. The basic approach uses the image gradient as an external force to attract the active contour to the object boundary (Kass et al., 1988). More sophisticated approaches offer successive refinements from coarse to fine segmentation (Nagappan et al., 2008). Several authors have offered the possibility of coupling these refinements with wavelet transforms (Nagappan et al., 2008; Shan and Ma, 2010). For example, the model in (Dah Way et al., 2005; Zhang and Liu, 2005) reduces computation time thanks to the multi-scale analysis nature of the wavelet transforms. In this case, because of their different singularities, signals and noise are easily distinguished by the local maxima of their coefficients. Wavelet Vector Flow (WVF) was then compared with a classic Gradient Vector Flow (GVF) and showed to be effective on few medical images segmentation (Cheng et al., 2007). Therefore, as wavelet transform has been widely and successfully used to capture multi-scale edges in medical images (Wang and Yang, 2007), we propose to evaluate its performance in wood slice images for the purpose of tree-ring delineation. We opted for a relatively recent enhancement of the Discrete Wavelet Transform (DWT) called the Q-*Shift* Dual Tree Complex Wavelet transform (DT-CWT) because of its near shift invariance and its frequency analysis qualities (Kingsbury, 2001). DT-CWT has already been successfully used in the level set approach (De Rivaz and Kingsbury, 2000) where it represented surface areas by complex coefficients derived from the transformation. In our snake approach, we introduce a new external force based on a feature derived from the DT-CWT: the Inter Coefficient Product (ICP) extracted from the DT-CWT which provides efficient features suitable for an active contour strategy by yielding edge orientations in the filter support regions (Anderson et al., 2005). We then summarize the different scales and orientation sub-band features provided by the transform into a single gradient-map that can be used as an attractor-map to design the external force.

Our contribution is therefore as follows:

- We propose a new approach for coupling the Q-*Shift* Dual Tree Complex Wavelet Transform and the point-based active contour model, and more particularly propose a formulation of the external force based on the magnitudes and orientations given by the ICP.

- We introduce different notions, such as attraction power and attraction orientation, which can be used to determine the most appropriate attractors and thereby simulate an external force field that results in rapid convergence to the balanced position.
- We describe and test a new method to delineate successive concentric tree-rings in *Abies alba* flatbed-scanned images by running successive active contour delineating tree-rings and inter tree-rings alternately.

2. Description of the method

2.1. The Dual-Tree Complex Wavelet Transform (DT-CWT)

In matters of texture image analysis and synthesis, the Q-*Shift* Dual-Tree Complex Wavelet Transform (DT-CWT) (Kingsbury, 2001), originating from the wavelet community, has proven to be superior to all other wavelet transforms (De Rivaz, 2000; Lo et al., 2011). The DT-CWT proposed by Kingsbury in (Kingsbury, 2001) is a relatively recent enhancement of the Discrete Wavelet Transform (DWT) where the DWT is considered to be one of the most useful mathematical tools for multi-resolution image analysis (Mallat, 1989). DWT aims to break down (decompose) a signal into a decimated multi-scale representation that isolates coarse image components into a sparse set of coefficients. It has been used in a wide range of applications for handling object detection, and image de-noising, compression and segmentation (Lu et al., 1997; Kim and Kang, 2007). The DT-CWT comes with several desirable properties for feature extraction: these transforms have similar shapes to Gabor wavelets (De Rivaz, 2000), with important properties additional to the DWT. It exhibits approximate shift invariance, is directionally selective ($\pi/10$, $\pi/4$, $2\pi/5$, $3\pi/5$, $3\pi/4$, $9\pi/10$ *vs* 0, $\pi/2$ and $3\pi/4$ for the DWT) and achieves perfect reconstruction along with good frequency localization. The main advantages of the DT-CWT over Gabor wavelets and other separable filter banks are limited redundancy and greater computational efficiency.

The 1-dimensional DT-CWT is implemented by using a pair of filter banks that process the input signal simultaneously. One tree produces the real and the other the imaginary part of the complex coefficient. For the 2-dimensional DT-CWT, which is similar to a 2-dimensional DWT, the tree pair is applied to the rows then the columns of the input image. This operation results in six complex high-pass sub-sampled sub-bands and one real low-pass sub-band at each level. Ultimately, the size of the final sub-bands is $1/2^k$ the size of the original signal for a k-level DT-CWT decomposition. Fig. 1a presents the impulse responses of the six complex wavelets associated with 2-D analysis filters.

2.2. Defining features using Inter Coefficient Products (ICP) from the DT-CWT

A relatively simple and computationally efficient representation of the coefficient phases of the DT-CWT coefficients provided access to the angles of dominant directional features in their support regions. These consist of the so-called Inter Coefficient Products (ICP) (Anderson et al., 2005) which are computed by measuring the relative phase of appropriate neighbor coefficients for the oriented sub-bands considered. These ICP coefficients are then used to construct Texture Orientation Maps (TOM) as illustrated in Fig. 2. This new feature is used in (Vo and Oraintara, 2010) for texture classification and segmentation by characterizing ICP phase distribution.

In this work, we want to evaluate the potential benefits of ICP features as an external force for an active contour model. For this purpose, we summarize ICP features into a single texture

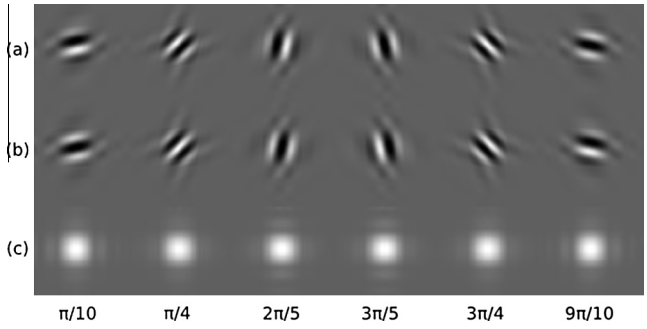

Fig. 1. DT-CWT impulse response filters: row (a) presents the real parts and row (b) the imaginary parts of complex filters, row (c) presents the magnitude of the filters.

orientation map which we then consider as a wavelet-based edge-map. The strategy provides a correct edge characterization of the image studied by merging the multi-scale edge analysis result from the DT-CWT. The proposed procedure is as follows:

1. Decompose the image to ψ by the N-level DT-CWT.
2. Compute ICP coefficients for each oriented sub-band of the n-levels.
3. Scale each sub-band to the size of the original image by interpolation. Note that this step is not necessary when using the undecimated version of the DT-CWT (Hill et al., 2012).
4. At each level, summarize the six oriented sub-bands to ψ_n (with n the scale level) by computing, at each location (x,y), the maximum value of ICP magnitudes over the six sub-bands and by keeping the corresponding phase value.
5. Summarize the N sub-bands obtained in step 4 to the final edge map ψ_f by computing, at each location (x,y), the vector sum of each complex coefficient by:

$$\arg(\psi_f(x,y)) = \arg\left(\sum_n^N (|\psi_n(x,y)| \times \arg(\psi_n(x,y)))\right)$$

$$|\psi_f(x,y)| = \sum_n^N |\psi_n(x,y)|$$

The orientations and magnitudes found at each level of the decomposition (step 4) are summarized in step 5 with the aim of using the most relevant orientation in the final features map. Thus, the proposed vector product considers the N orientations weighted by their corresponding magnitudes. This results in a complex final map where the phase presents an optimal orientation map from the multi-scale analysis, and where the magnitude can be used as an attractor feature in subsequent sections. Fig. 3 illustrates these two maps considered for the remainder of the study on an *Abies alba* wood slice image sample; color images are converted into gray levels by averaging color canals before the gradient computation. Such a gradient map cannot be used directly for tree-ring delineation by thresholding high gradient values. Discontinuities and local contrast variations do not allow a correct segmentation so that an active contour process is used to fit the tree-ring gradient continuously.

2.3. Integrating the features in the active contour framework

For the active contour framework, we chose a point-based representation which was proposed by Delingette and Montagnat (2001). At a time t, the closed contour is defined by a list of n

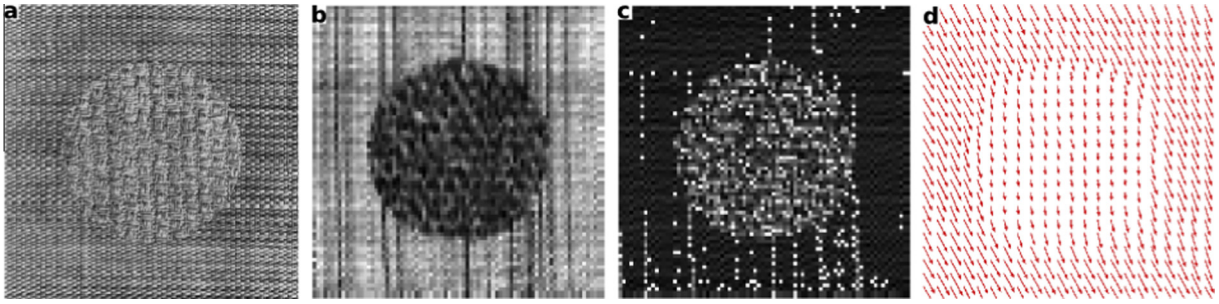

Fig. 2. ICP coefficients from the DT-CWT of image (a): (b) and (c) represent the magnitude and the phase of the complex coefficients at level 3 of the decomposition in the sub-band oriented at $2\pi/5$. In (d), local features are plotted as an arrow oriented according to phase, and are elongated according to magnitude.

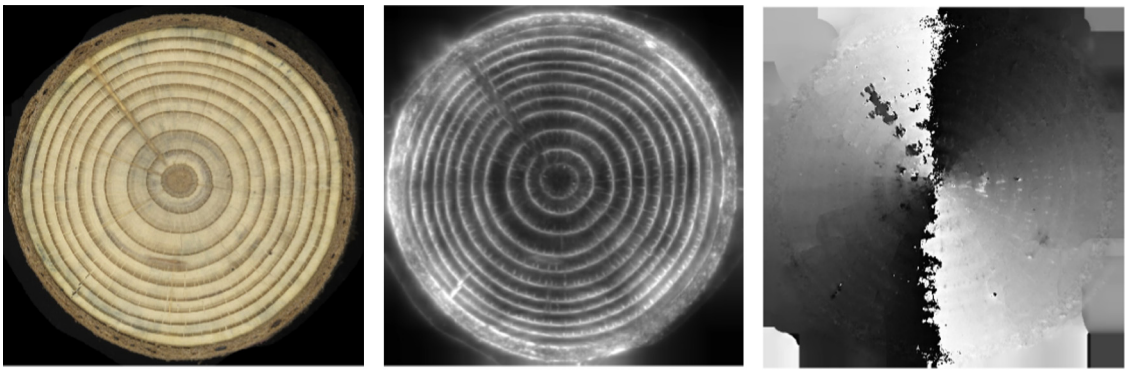

Fig. 3. Wood slice sample photographic image (a), with the magnitude map (b) (the histogram is stretched for visualization), and the orientation map (c) (gray levels represent angles comprised between $-\pi/2$ and $\pi/2$) obtained from the DT-CWT transform and the summary of ICP coefficients.

connected points P_i^t such that P_n^t is linked to P_1^t. The evolution of the active contour is then described by the equation:

$$P_i^{t+1} = P_i^t + (1-\gamma)\left(P_i^t - P_i^{t-1}\right) + \alpha_i \boldsymbol{Fint}_i^t + \beta_i \boldsymbol{Fext}_i^t \quad (1)$$

where α_i and β_i are respectively the weights for the internal and the external forces applied to point P_i^t and γ is a general damping term which allows oscillations to be avoided. In order to simplify the notation, in the remainder of this paper we write P_i (respectively $\boldsymbol{Fint}_i$, $\boldsymbol{Fext}_i$) instead of P_i^t (respectively $\boldsymbol{Fint}_i^t$, $\boldsymbol{Fext}_i^t$) for the vertex position at time t.

The internal function $\boldsymbol{Fint}_i$, regularizes the positions of the points with respect to the others through the following equation:

$$\boldsymbol{Fint}_i = \epsilon_i P_{i-1} + (1-\epsilon_i) P_{i+1} + L(r_i, \varphi_i^*, \epsilon i)\boldsymbol{n_i} \quad (2)$$

where

- ε_i and $(1-\varepsilon_i)$ are the barycentric coordinates of the projection of P_i onto the line $[P_{i-1}, P_{i+1}]$.
- r_i is the half distance between the two neighbors P_{i-1} and P_{i+1} of P_i.
- φ_i^* is the oriented simplex angle which gives the continuity constraint. It is defined as follows

$$\varphi_i^* = \sum_{j=i-s}^{j=i+s} \frac{\varphi_j}{(2s+1)}$$

  φ_j being the oriented angle between the two segments $[P_{j-1},P_j]$ and $[P_j,P_{j+1}]$, and s the coefficient of rigidity. It defines the smoothing of the snake.
- n_i is the local unit contour normal vector, and is oriented toward the exterior.

In Eq. (2), the function $L(\,)$ is given by the following expression:

$$L(r_i, \varphi_i^*, \varepsilon_i) = \frac{r_i}{tan\varphi_i^*}\left(1 + \mu\sqrt{1 + 4\varepsilon_i(1-\varepsilon_i)tan^2\varphi_i^*}\right)$$

where

$$\mu = -1 \text{ if } |\varphi_i| < \pi/2 \quad \text{and} \quad \mu = 1 \text{ if } |\varphi_i| > \pi/2$$

L is the normal component of the internal force and fixes the elasticity of the snake. When consecutive points of the snake are aligned, φ_i is nil and the L term is arbitrarily set to zero.

The external force $\boldsymbol{Fext}_i$ in Eq. (1), at point P_i, can be defined as an attraction force toward a point called the attractor and called A_i. $\boldsymbol{Fext}_i$ is defined as energy due to the interaction of the snake with the image. The definition of A_i is closely related to the application. In our approach, we used the DT-CWT-based gradient described in the previous section. A_i is based on the magnitude and orientation maps given by the DT-CWT. The aim is to find attractors, i.e. sufficiently strong local maxima on the magnitude map, along the directions locally given by the orientation map. Once A_i is established (see next section), the $(P_i\,A_i)$ couple forms a normalized vector which is weighted by the unit coefficient determined from a mean combination between the distance and intensity of the attractor. The external force decreases as point P_i converges toward its balanced position.

In the point-based active contour, the external function $\boldsymbol{Fext}_i$ is as follows:

$$\forall i \in \{1,\ldots,n\} \boldsymbol{Fext}_i = \frac{1}{2}\left(\Delta v_i + \frac{|d_i|}{d_{max}}\right)\boldsymbol{w_i}$$

where

- Δv_i is the unit value difference, or magnitude difference (derived from the DT-CWT-based gradient) between P_i and its attractor A_i. It should be noted that these magnitudes are values scaled between 0 and 1. d_i is the signed distance between P_i and its attractor A_i: d_i is positive when A_i is outside the contour and negative when it is inside. d_{max} is a parameter that regulates the distance maximum beyond which attraction is considered to be nil.
- w_i is the unit attraction vector; it is conventionally defined in the literature as the normal vector on the P_i position oriented to the exterior of the contour. Here, we define it as the weighting vector sum

$$\boldsymbol{w_i} = (1 - v_i)\boldsymbol{n_i} + v_i\boldsymbol{o_i}$$

  o_i is the unit vector given by the orientation map. It gives the direction of the closest contour detected by the wavelets. When the v_i magnitude at the P_i position is nil or too weak, the attraction occurs along the normal vector n_i to the snake; when the v_i magnitude is well tagged, the attraction occurs along the orientation given by the wavelets. This vector sum simulates a force field without any extrapolation or diffusion of the values given by the DT-CWT orientation map.

Finally, $\boldsymbol{F}_{ext}$ is designed such that the greater the potential difference is between P_i and its attractor A_i, the stronger the attraction is, and such that the greater the distance is between P_i and its attractor A_i, the weaker the attraction is.

The potential A_i points along the attraction axis are defined as the most attractive local maxima computed in a mask of a given length k on both sides of the contour, and allow both internal and external displacements.

An attraction power is calculated for each potential attractor A_i found, and is related to the current position P_i. The final selected attractor is that which has the greatest attraction. Attraction power pa is a signed coefficient that expresses the following idea: attraction decreases as the distance between the point and its attractor increases; attraction increases as the intensity difference between the point and its attractor increases. The attraction power function thus depends on the positions and magnitudes of compared points (by convention, the attraction power of two superimposed points is nil). This definition is used to choose the most appropriate attractor when several local maxima are found on both sides of the contour. Attraction power is defined by the following expression:

$$\forall\, P_i \neq P_j \; pa_{ij} = \frac{v_i - v_j}{\|P_iP_j\|}$$

The result of our method is a polygonal line $[P_0, P_i, P_n]$ which represents a tree-ring delimitation. This polygonal line can be transformed into a closed 8-connected relationship contour in the image.

2.4. Application to tree-ring delineation

The proposed method was used to detect tree-rings in images of *Abies alba* wood slices. Tree-rings were delineated from the bark to the pith. We have seen that a tree-ring corresponds to a sudden transition between a light and a dark area and that its boundary corresponds to the highest values in the gradient-map. The idea was therefore to start the active contour in a light area, i.e. corresponding to the lowest magnitude values in the gradient-map, located around a tree-ring, in order that the external force defined in Section 2.3 could be effective. Of course, to avoid any ambiguity, it was essential to remove from the gradient map any external magnitudes which could also attract the active contour. For this purpose, we first initialized manually the active contour along the wood slice border and let it converge toward the first tree-ring. Then, iteratively (1) we changed the external force by taking the minimal values in the gradient-map which corresponded to the so-called inter tree-ring position and we let the active contour converge toward this area (see Fig. 4, in blue), (2) we set to zero all magnitudes of the gradient-map which were external to the current position of the active contour which was now stabilized around a tree-ring, (3) we used the external force defined in Section 2.3 in order that the active contour could move toward the next (internal) tree-ring (see Fig. 4, in red). The process allowed us to delineate tree-rings from the bark to the pith for an entire wood slice image as shown in Fig. 5 on a 48-year-old *Abies alba* wood slice. The method takes a reasonable average time of around 5 min. on a standard machine depending mostly on the image resolution, the number of tree-rings, the number of contour's points and the image complexity (in term of structure and intensity). Note that the tree-ring search was stopped when the pith was encountered, i.e. when the inner distribution variance of the contour reached a given threshold. More robust constraints could be envisaged either on the contour (radius, perimeter, surface, etc.) or on its image/gradient domain (statistics, texture, etc.). As well, an automated initialization of the active contour around the first tree-ring could be envisaged for example by background and bark detection.

3. Results

3.1. Application to Abies alba wood slice images

When applied to tree-ring delineation, our method yielded accurate results as seen in Fig. 5. In particular, the active contour adopted the expected position for tree-ring delineation even when some wood defects were present. Fig. 6 shows the results around branch insertions (Fig. 6a and d), knots (Fig. 6c) and small and medium cracks resulting from log drying (Fig. 6d and b, respectively).

3.2. Evaluation metric

In order to assess the method with respect to contours delineated by experts, to analyze the influence of some parameters or to quantify sensitivity to image noise, we had to compare different pixel contours for a given tree-ring. But, we could not just study the overlapping of contours as, for example, two co-circular contours shifted by only one pixel may not have shared any pixel. This demonstrates the need to introduce a margin error to consider that two or more contours are identical (or at least consistent). For example, pixels can be put in correspondences between contours via a min-cost assignment method on a bipartite graph and given a margin error (Scott and Nowak, 2006). However, we opted for a global geometrical approach to avoid the pixel matching procedure which is complex. Our comparison between two contours was based on the overlapping of regions which were created by thickening each contour. For this purpose, we applied to each contour a mathematical morphology operator called dilation, which consists in aggregating pixels in the neighborhood of the existing pixels. If we performed n dilations, the contour had a thickness of $2n + 1$ pixels which defined the region corresponding to a margin error of n.

Hence we were able to define Precision/Recall measurements. First, we defined gt and s as, respectively, the contour which was considered as ground truth (in general, the tree-ring delineated by an expert) and the one given by our method. We were then able to compute, $gt_d(n)$ and $s_d(n)$, which were the same contours after n dilations. Then, we defined True Positives as $\mathrm{TP} = s \cap gt_d$, Falses

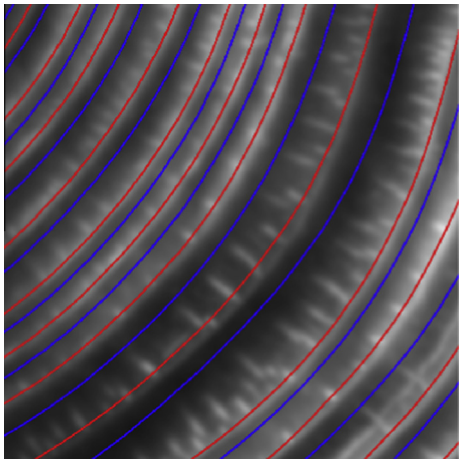

Fig. 4. Successive delineations of tree-rings (in red) and inter tree-rings (in blue) using our method. Tree-rings (respectively inter tree-rings) are given by the active contours which are stabilized on local maxima (respectively local minima) in the displayed gradient-map. (For interpretation of the references to colour in this figure legend, the reader is referred to the web version of this article.)

Positives as $FP = s \setminus TP$, True Negatives as $TN = s_d \cap gt_d$ and False Negatives as $FN = s_d^c \cap gt$. Finally, the Precision measurement was given by $P = TP/(TP + FP)$, the Recall measurement by $R = TP/(TP + FN)$ and the *F*-score by $F = 2PR/(P + R)$. In the following, we use the *F*-score, which provides a balanced average of the Precision and Recall ranged between 0 (worst score) and 1 (best score), to characterize the quality of tree-ring delineations.

TP, FP, TN and FN depend on the margin error *n*. A large margin error provides good detection scores, which may be not significant for experts, whereas too small a margin error always results in poor detection scores. Thus, *n* has to be calibrated with great care. For this purpose, three different experts delineated manually the same 5 rings of an *Abies alba* image by using the same functionalities of the same software, ImageJ (Rasband, 1997–2014) and by following the same protocol (e.g. zoom level during annotation, approximate space between points of the polygonal line, etc.). The idea was that a significant margin error to assess our method should be in the range of the average inter-expert error. As we did not know the exact contour of a tree ring, we compared all the pairs of contours given by the experts. For one tree-ring (and a given *n*), we therefore had 6 *F*-scores that were averaged. We present in Fig. 7a the evolution of the mean *F*-score in line with the margin error *n* (in pixels). If we assumed that a mean *F*-score of ~0.9 showed a good agreement between the 3 experts, we found that we had to select a margin error of $n = 6$ pixels, which corresponded to 0.4 mm in the image (see an illustration of this margin in the case of delineation by two experts in Fig. 7b). We used this value for the assessment of all the following experiments since our images had similar resolutions.

3.3. Evaluation of the DT-CWT-based gradient

We chose *a priori* the DT-CWT for (1) its multi-resolution ability to provide relevant magnitudes in a wide range of tree-rings combined with (2) computing ICP which are efficient in providing accurate edge (or tree-ring transition) orientations on extensive areas, (3) while being robust to noise. In this section, we address

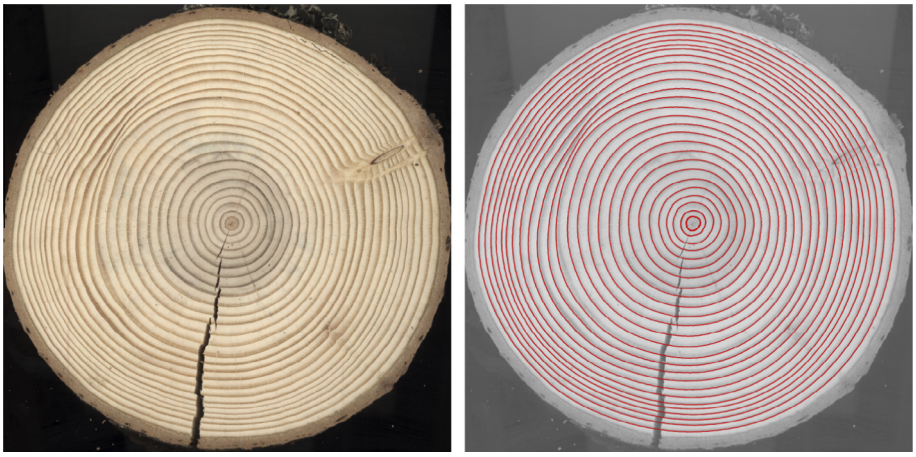

Fig. 5. Full delineation of tree-rings on an image of a 46-year-old *Abies alba* wood slice. The parameters of the snake were set as: number of points = 300, $\alpha = 0.5$, $\beta = 0.5$, $k = 50$.

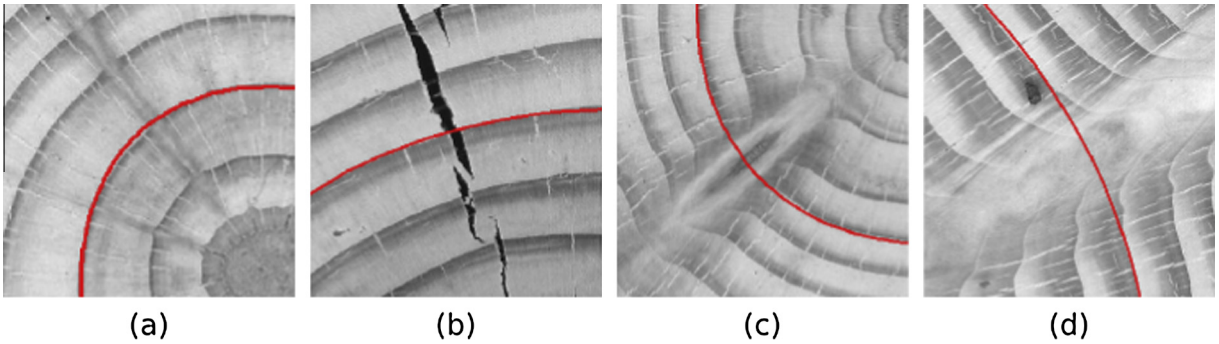

Fig. 6. Our method succeeded in delineating accurate tree-rings even in the presence of defects such as branch prints (a,d), cracks (b,d) and knots (c).

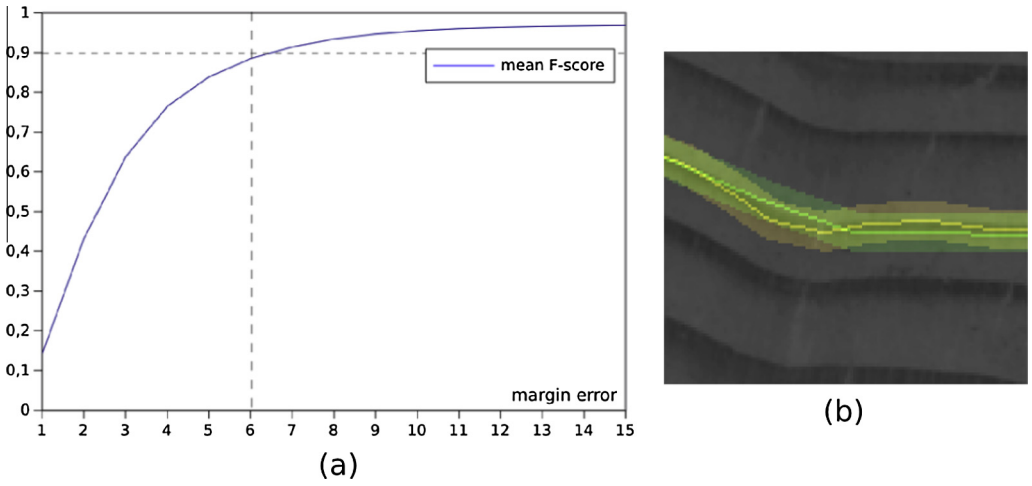

Fig. 7. (a) Mean *F*-score resulting from the delineations made by 3 different experts on the same 5 tree-rings. The margin error corresponds to the number of dilations n applied on the discrete contours in order to compute the TP, TN, FP and FN coefficients; (b) margin error (with $n = 6$) on two expert delineations, in yellow and green respectively. (For interpretation of the references to colour in this figure legend, the reader is referred to the web version of this article.)

the relevance of the DT-CWT-based gradient with respect to more standard features. For this purpose, we applied the proposed DT-CWT procedure, as well as the classic Sobel operator, on the wood slice presented in Fig. 3. First, we took a 1-dimensional radial profile from the bark to the pith and we present in Fig. 8 the original intensity profile (upper row), the Sobel gradient magnitude (middle row) and the DT-CWT-based gradient magnitude (bottom row). In addition, both gradient orientations can be seen in light gray. It can be seen that the DT-CWT gradient is much smoother than the Sobel gradient, avoiding high magnitude values resulting from local noise. Furthermore, in a radial cross-section, tree-ring transitions are expected to be oriented similarly as they are quite concentric in (Fig. 3). Indeed, we obtained a near constant DT-CWT gradient orientation, which was expected for an accurate guidance of the active contour.

Hence, the Sobel gradient is very sensitive to noise; if it is to be used to define an external force for the active contour, a blurring filter needs to be applied on its magnitude map. This reduces the influence of the noise but at the cost of some loss of precision in the maxima coordinates. Without a blurring step, the Sobel gradient delivers high magnitudes that are too imprecise and misplaced so that it is not possible to process the entire wood slice from bark to pith with successive delineations as described in Section 3.1.

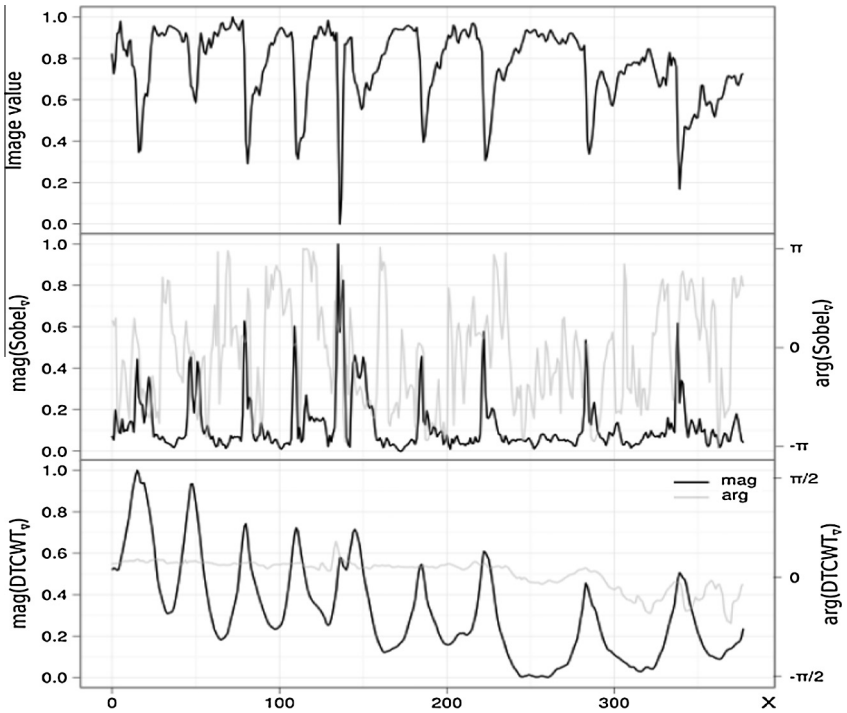

Fig. 8. Results on a1-dimensional radial profile from bark to pith extracted from the wood slice presented in Fig. 3. Upper row: original intensity profile. Middle and bottom rows: Sobel gradient and DT-CWT-based gradient profiles, magnitudes are in black and orientations in gray. The DT-CWT-based gradient offers smoother values and delivers a near constant gradient orientation. In particular, around $x = 130$ there is a very deep and narrow valley in the original intensity profile which characterizes a punctual noise. At this value, the Sobel magnitude is very high whereas the DT-CWT magnitude value remains stable, showing the robustness of the DT-CWT transform with respect to noise.

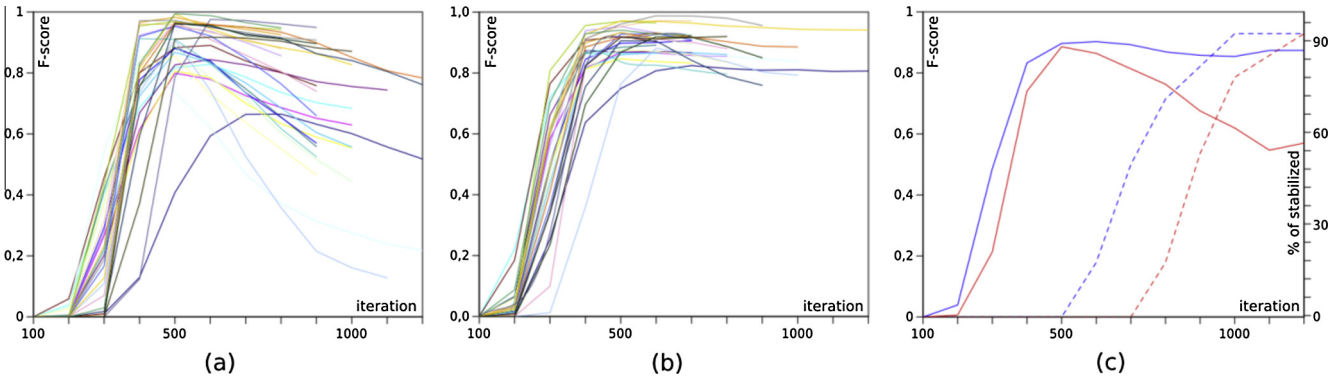

Fig. 9. Evolution of *F*-score with respect to the number of iterations for several snakes with the Sobel-based gradient (a) and DT-CWT-based gradient (b). In (c), the corresponding mean *F*-score evolution for both gradients (Sobel with continuous red line and DT-CWT with continuous blue line); in addition, the percentage of stabilized snakes for the Sobel-based gradient (with dashed redline) and DT-CWT-based gradient (with dashed blue line). (For interpretation of the references to colour in this figure legend, the reader is referred to the web version of this article.)

We then wanted to compare the accuracy of both gradients. Thus, we processed an entire wood slice and compared 28 tree-ring delineations based on the DT-CWT gradient and on the Sobel gradient. In both cases, we used strictly the same parameters for the active contour: the number of points was 300, $\alpha = 0.5$ and $\beta = 0.5$. The Sobel magnitudes map was blurred with a Gaussian kernel ($\delta = 12$) so that the successive tree-ring delineation process worked well. Our results showed a mean *F*-score of 0.88 ± 0.06 with the DT-CWT gradient and a mean *F*-score of 0.66 ± 0.22 with the Sobel gradient.

We present in Fig. 9 the *F*-scores of the 28 active contours at different steps (iterations) of their evolution until convergence. Both gradients, Fig. 9a and b for the Sobel and DT-CWT gradients respectively, are plotted. Additionally, we summarize in Fig. 9c the mean *F*-score evolution obtained for both gradients (in blue DT-CWT, in red Sobel) as well as the proportion of stabilized active contours (out of the 28): i.e. contours which reached their final position with no more moving points. First, it shows how the DT-CWT-based gradient outperformed the Sobel-based gradient in terms of delineation precision. Furthermore, it can be seen that the active contour stabilized much quicker with the DT-CWT gradient than with the Sobel-based gradient, e.g. at iteration 700, half of the active contours were stabilized with the DT-CWT-based gradient while none were with Sobel-based gradient. This resulted from the robust and relevant directions that were given by the phase of the DT-CWT-based gradient, as well as smooth magnitude values.

Finally, if we look at the Sobel-based active contour behaviors, we can see that most of them went through on relevant positions

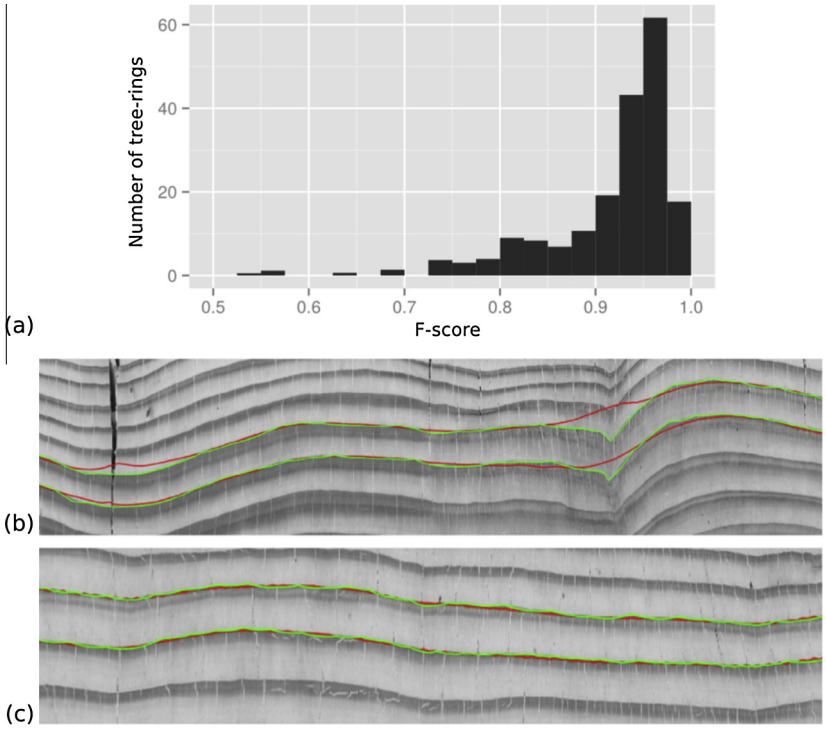

Fig. 10. (a) *F*-score distribution resulting from the automatic tree-ring delineation over the full set of seven *Abies alba* wood slices, for a total of 204 tree-ring delineations. (Min = 0.52, 1st Quartile = 0.89, Median = 0.94, Mean = 0.91, 3rd Quartile = 0.96, Max = 1.00). (b) Illustration of delineations scored low (*F*-score equal to 0.54 and 0.57) and (c) scored high (*F*-score equal to 0.87 and 0.92). Expert delineations are in green (b, c), automated delineations are in red. The illustrations show a transposed version of the original images after a polar transform in order to facilitate visual estimation. (For interpretation of the references to colour in this figure legend, the reader is referred to the web version of this article.)

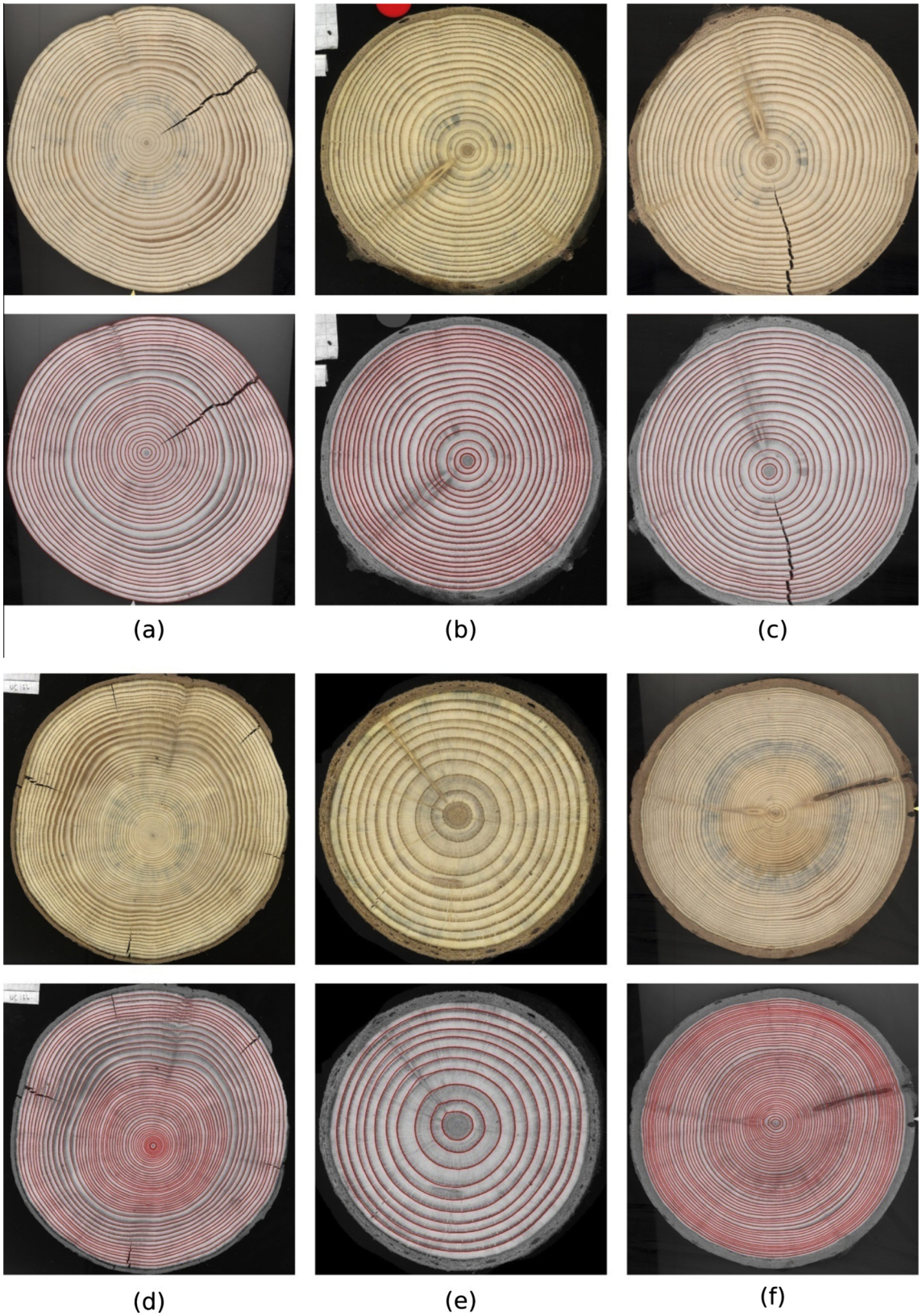

Fig. 11. Results of our method applied on six images of *Abies alba* wood slices of different ages presenting specific default structures such as branch prints, cracks, knots or mold.

(with high *F*-scores) but did not stabilize on them and continued on to wrong positions (with weaker *F*-scores). This was mainly due to high local maxima which were misplaced on the gradient-map (because of blurring or due to residual noise). On the other hand, DT-CWT-based delineations stabilized well on optimal localizations (see Fig. 10).

3.4. Comparison with expert measurements

To assess the suitability of our method, we asked experts (i.e. botanists specialized in wood anatomy) to manually annotate 7 images with different tree ages (from 10 to 50 years) and with several defects highlighted previously (cracks, mold prints, branch prints, non-circular tree-ring, etc.). We then obtained 204 ground-truth tree-rings. Fig. 11 illustrates our image set (except the one presented in Fig. 5) as well as the delineations resulting from the proposed method. In Fig. 10a, we can see the distribution of the *F*-score between the ground-truth contours and the contours given by our method. The accuracy yielded by our automatic method was comparable to that of the expert measurements with a mean *F*-score of 0.91 ± 0.08, considering a margin error of 6 pixels. These results highlight the accuracy of the method compared to the inter-expert error measured using the same margin-error (see Section 3.2); in most cases, our method delineated tree-rings with the same accuracy as an expert could have achieved. Fig. 10b,c illustrate samples of the automated delineation with the expert's delineation for two cases where *F*-scores reached by our automatic method were ∼0.55 and ∼0.90.

4. Discussion and conclusion

This study provides a full framework for automatically delineating tree-rings in photographic images, which may solve major problems in dendrology, including, among other things, the detection of structures such as knots (Longuetaud et al., 2012) and piths (Boukadida et al., 2012). The point-based active contour method chosen, coupled with a DT-CWT-based gradient, proved its capacity to delineate tree-rings in images of *Abies alba* wood slices. We assessed the precision of the automatic delineation method by providing encouraging Precision Recall measurements yielded between several automatically-delineated and expert-delineated tree-rings.

In most cases, contour initialization conditions are an important issue. Our method yielded good results by starting with normal orientations and appropriate ranges for maxima. However, improvements could be made by using a continuous vector flow approach that could be provided by the DT-CWT through a conventional diffusion process (Xu and Prince, 1998a,b; Cheng et al., 2007). This was not necessary in our particular context but it could be relevant in other fields. The comparison itself between Generalized GVF (Xu and Prince, 1998b) and our approach may be of interest in a more general context since we showed that ICP features can provide local vector flow. In our method, segmentation accuracy mainly depended on the gradient provided by the DT-CWT analysis. Multi-scale edge detection is another major issue in the field of computer vision. In our study, DT-CWT clearly demonstrated its ability to capture relevant contour localization on multiple scales and orientations. The merging scale solution proposed here is simple and efficient compared to the other methods we considered, such as reconstructing the image after setting low-pass coefficients to 0, or reconstructing the image while holding only local maxima in high-pass coefficients (Mallat and Zhong, 1992). However, the number of scales to be considered for the transform is an open question. We systematically used 6 levels of decomposition in this study but the precision of local maxima localization is directly affected by this parameter. Other wavelet transforms could be considered in this context, particularly the contourlet and shearlet transforms (Wang and Yang, 2007), which deal efficiently with edge localization.

The point-based active contour method employed in this study has several advantages in the delineation of tree-rings. In particular, it is simple to parameterize. For example, contour rigidity is simply tuned by the number of points and the stop condition is determined by the number of moving points and/or the maximal number of iterations. Vertex spacing is controlled through the tangential component of the internal force applied to each vertex and we opted for an equidistant spatial distribution in order to constrain the distance between successive vertices. Internal force expression does not depend on contour parameterization: it regularizes the contour curvature without producing shrinkage. Such a point-based active contour could also manage topology changes: (Delingette and Montagnat, 2001) proposed an algorithm that creates and merges different connected components of the contour based on the detection of edge intersections. In particular, this should be of particular usefulness for processing wood slices with several piths. Moreover, as no lengthy global minimization calculations are necessary to determine an optimal "stabilized" position, the convergence process remains fast.

We developed a method that can deal with *Abies alba* wood slice images. But the complexity of the content in such images varies and mainly depends on the type of wood analyzed and the image acquisition system. Particular wood cell types may be more pronounced (e.g. rays and vessels) and can disturb the tree-ring delineation method. An important issue in this context is also to deal with branch insertions, off-centered second pith, false tree-rings, knots and confused tree-rings. In the last case, the successive tree-ring and inter tree-ring detection process described here could run into problems due to irregular annual (or periodic) wood growth. Ways of improvement may reside in the *a priori* detection of these particular wood cells and structures, depending on the species, in order either to adapt gradient computation or the active contour evolution scheme.

Note

We provide, as supplementary materials, our set of images as well as expert delineations and our delineation results. The proposed method will be available in the TOASTER[2] platform.

Acknowledgments

We wish to thank O. Taugourdeau for providing the *Abies alba* wood slice images (wood slices were prepared and photographed by P. Cretin-Maitenaz and the INRA-URFM technical team) and M. Jones for assistance with the preparation of the manuscript.

Appendix A. Supplementary material

Supplementary data associated with this article can be found, in the online version, at http://dx.doi.org/10.1016/j.compag.2015.09.009.

References

Anderson, R., Kingsbury, N., et al., 2005. Determining multiscale image feature angles from complex wavelet phases. Comput. Sci. 3656, 490–498.
Bhandarkar, S.M., Luo, X., et al., 2005. Detection of cracks in computer tomography images of logs. Pattern Recogn. Lett. 26 (14), 2282–2294.
Borianne, P., Pernaudat, R., et al., 2010. Automated delineation of tree-rings in X-Ray computed tomography images of wood. In: 2011 18th IEEE International Conference on Image Processing (ICIP).
Boukadida, H., Longuetaud, F., et al., 2012. PithExtract: a robust algorithm for pith detection in computer tomography images of wood – application to 125 logs from 17 tree species. Comput. Electron. Agric. 85, 90–98.
Cai, H., Xu, X., et al., 2006. Repulsive force based snake model to segment and track neuronal axons in 3D microscopy image stacks. NeuroImage 32 (4), 1608–1620.
Caselles, V., Catté, F., et al., 1993. A geometric model for active contours in image processing. Numer. Math. 66 (1), 1–31.

[2] http://amap-collaboratif.cirad.fr/pages_logiciels/index.php?page=toaster.

Cerda, M., Hitschfeld-Kahler, N., et al., 2007. Robust tree-ring detection. Advances in Image and Video Technology. Second Pacific Rim Symposium, PSIVT 2007, Santiago, Chile, December 17–19. Springer.

Chalifour, A., Nouboud, F., Deprost, B., Okana S., 2001. Automatic detection of tree-rings on wood slice images. In: 5th International Conference on Quality Control by Artificial Vision, Le Creusot France.

Chen, S., Sochen, N.A., et al., 2006. Integrated active contours for texture segmentation. IEEE Trans. Image Process. 15 (6), 1633–1646.

Cheng, J., Liu, Y., et al., 2007. A new active contour model for medical image analysis – wavelet vector flow. Int. J. Appl. Math. 36.

Conner, W.S., Schowengerdt, R.A., et al., 1998. Design of a computer vision based tree ring dating system. In: IEEE Southwest Symposium on, Image Analysis and Interpretation, 1998.

Dah Way, F., Rajeswari, M. et al., 2005. Segmentation using wavelet and GVF snake. ACIT – Signal and Image Processing. Novosibirsk, Russia.

De Rivaz, P., 2000. Complex Wavelet Based Image Analysis and Synthesis. University of Cambridge.

De Rivaz, P., Kingsbury, N., 2000. Fast segmentation using level set curves of complex wavelet surfaces. In: Proceedings, 2000 International Conference on, Image Processing, 2000.

Delingette, H., Montagnat, J., 2001. Shape and topology constraints on parametric active contours. Comput. Vis. Image Underst. 83 (2), 140–171.

Gao, J., Kosaka, A., et al., 1998. A deformable model for human organ extraction. In: Proceedings, 1998 International Conference on, Image Processing, 1998, ICIP 98.

Giraldi, G., Suri, J., et al., 2006. Implicit dual snakes for medical imaging. Conf. Proc. IEEE Eng. Med. Biol. Soc. 1 (1), 3025–3028.

Hanning, T., Kickingereder, R., et al., 2003. Determining the average annual ring width on the front side of lumber.

He, L., Peng, Z., et al., 2008. A comparative study of deformable contour methods on medical image segmentation. Image Vis. Comput. 26 (2), 141–163.

Hill, P., Achim, A., et al., 2012. The Undecimated Dual Tree Complex Wavelet Transform and its application to bivariate image denoising using a Cauchy model. In: 2012 19th IEEE International Conference on Image Processing (ICIP), Orlando, USA.

Kass, M., Witkin, A., et al., 1988. Snakes: active contour models. Int. J. Comput. Vision 1 (4), 321–331.

Kim, S.C., Kang, T.J., 2007. Texture classification and segmentation using wavelet packet frame and gaussian mixture model. Pattern Recogn. 40 (4), 1207–1221.

Kingsbury, N.G., 2001. Complex wavelets for shift invariant analysis and filtering of signals. Appl. Comput. Harmonic Anal. 10 (3), 234–253.

Kumpulainen, P., Marjanen, K., 2010. Directional variance analysis of annual rings. J. Phys: Conf. Ser. 238 (1), 012047.

Lo, E.H.S., Pickering, M.R., et al., 2011. Image segmentation from scale and rotation invariant texture features from the double dyadic dual-tree complex wavelet transform. Image Vis. Comput. 29 (1), 15–28.

Longuetaud, F., Mothe, F., et al., 2012. Automatic knot detection and measurements from X-ray CT images of wood: a review and validation of an improved algorithm on softwood samples. Comput. Electron. Agric. 85, 77–89.

Lu, C.S., Chung, P.C., et al., 1997. Unsupervised texture segmentation via wavelet transform. Pattern Recogn. 30 (5), 729–742.

MacDonald, G.M., 1998. Tree rings and environment: dendroecology. By F.H. Schweingruber. New Phytol. 138 (4), 743–750.

Malladi, R., Sethian, J.A., et al., 1995. Shape modeling with front propagation: a level set approach. IEEE Trans. Pattern Anal. Mach. Intell. 17 (2), 158–175.

Mallat, S., Zhong, S., 1992. Characterization of signals from multiscale edges. IEEE Trans. Pattern Anal. Mach. Intell. 14 (7), 710–732.

Mallat, S.G., 1989. A theory for multiresolution signal decomposition: the wavelet representation. IEEE Trans. Pattern Anal. Mach. Intell. 11 (7), 674–693.

McInerney, T., Terzopoulos, D., 1996. Deformable models in medical image analysis: a survey. Med. Image Anal. 1 (2), 91–108. http://dx.doi.org/10.1016/S1361-8415(96)80007-7, ISSN: 1361–8415.

Nagappan, A., Prabhu Britto, A., et al., 2008. Novel segmentation technique using wavelet based active contour model for detection of mammographic lesions. Inf. Technol. J. 7, 490–496.

Norell, K., 2011. Automatic counting of annual rings on Pinus sylvestris end faces in sawmill industry. Comput. Electron. Agric. 75 (2), 231–237.

Paragios, N., Deriche, R., 2000. Geodesic active contours and level sets for the detection and tracking of moving objects. IEEE Trans. Pattern Anal. Mach. Intell. 22 (3), 266–280.

Rasband, W.S., 1997–2014. ImageJ. USA, U.S. National Institutes of Health.

Scott, C., Nowak, R., 2006. Robust contour matching via the order-preserving assignment problem. IEEE Trans. Image Process. 15 (7), 1831–1838.

Shan, H., Ma, J., 2010. Curvelet-based geodesic snakes for image segmentation with multiple objects. Pattern Recogn. Lett. 31 (5), 355–360.

Sjöberg, P.-J., Danielsson, P.-E., et al., 2001. Image analysis of annual ring pattern for prediction of wood quality. In: Symposium on Image Analysis, Norrpöking, Sweden.

Soille, P., Misson, L., 2001. Tree ring area measurements using morphological image analysis. Can. J. For. Res. 31 (6), 1074–1083.

Suri, J.S., Kecheng, L., et al., 2002. Shape recovery algorithms using level sets in 2-D/3-D medical imagery: a state-of-the-art review. IEEE Trans. Inf. Technol. Biomed. 6 (1), 8–28.

Tadeusz, S., Morel, O., et al., 2003. Detection automatique des stries de croissance des arbres par transformÃ©e en ondelettes. CNRIUT.

Vaz, C., Carvalho, P., et al., 2004. A vision-based system for automatic growing ring detection and measurement. Comput. Ind. Eng. 46 (2), 347–354.

Vo, A., Oraintara, S., 2010. A study of relative phase in complex wavelet domain: property, statistics and applications in texture image retrieval and segmentation. Signal Process.: Image Commun. 25 (1), 28–46.

Wang, P.S.P., Yang, J., 2007. A review of wavelet-based edge detection methods. Int. J. Pattern Recognit Artif Intell. 26 (07), 1255011.

Xu, C., Prince, J.L., 1998a. Snakes, shapes, and gradient vector flow. IEEE Trans. Image Process. 7 (3), 359–369.

Xu, C., Prince, J.L., 1998b. Generalized gradient vector flow external forces for active contours. Signal Process. 71 (2), 131–139.

Zhang, H.-W., Liu, Z.-G., 2005. Wavelet-based snake model for image segmentation. In: Proc. of SPIE 6044, pp. 604420-604420.